

# The competing effects of stress and water saturation on *in situ* $Q$ for shallow (< 1 m), unconsolidated sand, evaluated with a modified spectral ratio method

James M. Crane<sup>1</sup>, Juan M. Lorenzo<sup>1\*</sup>, Jie Shen<sup>1</sup> and Chris D. White<sup>2</sup>

<sup>1</sup>Department of Geology & Geophysics, Louisiana State University, Baton Rouge, LA 70803, USA

<sup>2</sup>Department of Earth & Environmental Sciences, Tulane University, New Orleans, LA 70118, USA

Received August 2016, revision accepted September 2017

## ABSTRACT

A publicly available seismic dataset from a lab experiment shows the simultaneous dependence of quality factor ( $Q$ ) on water saturation and stress in unconsolidated sand. Large  $Q$  gradients (e.g.,  $> 10 \text{ m}^{-1}$ ) necessitate a spectral ratio method modified to assume that  $Q$  changes with each ray path, thereby eliminating false  $Q$  values (e.g.,  $< 0$ ). Interval  $Q$  values ( $Q_{int}$ ) increase the most with depth ( $dQ/dz = 43 \text{ m}^{-1}$ ) and stress ( $dQ/d\sigma = 0.0025/\text{Pa}$ ) in dry sand and the least in partially saturated sand ( $dQ/dz = 10 \text{ m}^{-1}$  and  $dQ/d\sigma = 0.0013/\text{Pa}$ ) where attenuation created by local fluid flow reaches a maximum. Expected  $Q_{int}$  values can be extrapolated from  $dQ/d\sigma$  and are bounded by  $Q_{int}$  of the dry ( $Q_{dry}$ ) and partially saturated ( $Q_{wet}$ ) media (e.g.,  $Q_{dry} \geq Q_{int} \geq Q_{wet}$ ).  $Q_{int}$  deviations outside this range may be explained by changes in effective stress, attenuation mechanism, or sediment composition. Field values of seismic attenuation in natural settings may be helped by these constraints, although attenuation remains subject to careful consideration of other factors, e.g., grain size, sorting, and shape.

## INTRODUCTION

Field investigations into the simultaneous effects of water saturation and stress on seismic attenuation have yet to be accomplished, despite many core samples (Winkler and Nur 1982; Cadoret, Mavko and Zinszner 1998) and theoretical studies (Biot 1956; Pham *et al.* 2002). A field-transferrable lab experiment focusing on these relationships may produce useful estimates of seismic attenuation that can be used to constrain field values of water saturation and stress. The ability to estimate water saturation with seismic methods would be particularly important in better constraining hydrogeological studies (Arnold *et al.* 1998; Binley *et al.* 2001) or reservoir management (Thakur 1991), both of which implement water-saturation sensitive calculations.

Whereas velocity analysis will teach us much about the elastic properties of soils, seismic attenuation can tell us much about the inelasticity, which can be equally important (Cadoret *et al.* 1998). Seismic waves lose energy during propagation for various reasons, including (i) geometric spreading as total energy is spread over an increasingly large wavefront (Cerveny, Langer and Pšenčík 1974); (ii) scattering as waves change phase (Wu and Aki 1988); and (iii) intrinsic attenuation as kinetic energy is permanently exchanged into heat (Wu 1985), as follows:

$$A(\omega) = cA_0(\omega)e^{-\alpha(\omega)x}, \quad (1)$$

\* glllore@lsu.edu

where  $\omega$  is the angular frequency of the seismic wave;  $A$  is the current amplitude;  $A_0$  is the initial amplitude;  $\alpha$  is the attenuation parameter, which represents the energy a wave loses while travelling a unit of distance;  $x$  is the distance travelled by the wave; and  $c$  is the frequency-independent attenuation usually attributed to geometric spreading. Moreover, the frequencies in our dataset ( $10^3 \text{ Hz}$ ) lie at the transition between high-frequency and low-frequency behaviours (Mavko, Mukerji and Dvorkin 2005) of well-known models for behaviour fluid–grain interaction and attenuation, such as squirt–flow (e.g., Mavko and Nur 1975) and Biot theory (1956).

Because attenuation is dependent on both the distance travelled and the number of oscillations during propagation, it is convenient to describe attenuation by the energy lost per oscillation, which is the inverse of the seismic quality factor ( $Q$ ) (Knopoff 1964), as follows:

$$Q^{-1} = \frac{\Delta E}{2\pi E}, \quad (2)$$

where  $\Delta E$  is the energy dissipated during one cycle of loading at a circular frequency and  $E$  is the maximum energy stored during that cycle—where  $Q$  is large, attenuation is small, and vice versa. Attenuation caused by scattering can be dismissed when the propagating wavelength is much larger than heterogeneities.

The relationship between  $Q$  and  $\alpha$  has been shown (Futterman 1962) as follows:

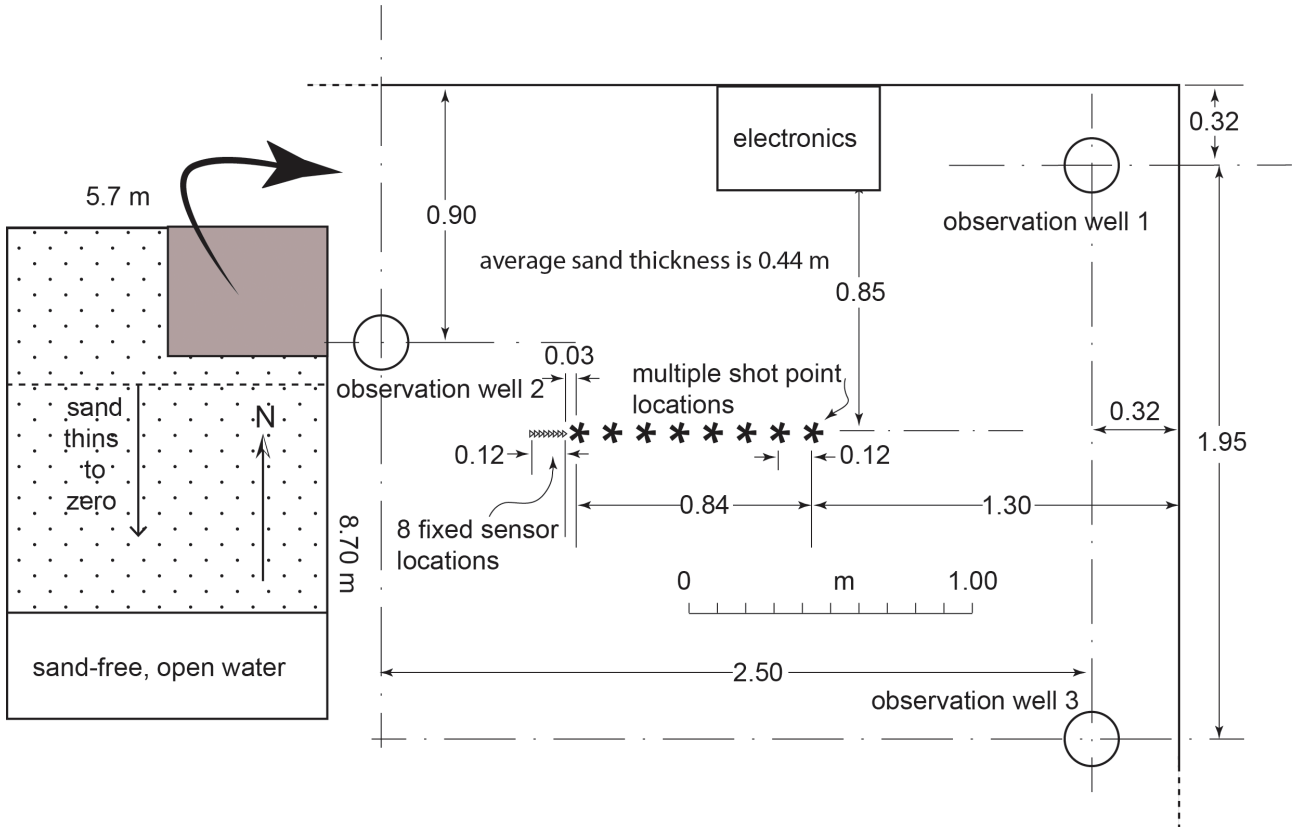


**Figure 1** Map layout of seismic acquisition equipment and observation wells in sand tank (Lorenzo *et al.* 2013). Pseudo-walkaway experiment is set up in a 0.44-m-thick section of sand at least 0.85 m away from the nearest wall in an east–west orientation. Sand surface is leveled prior to data acquisition. Sensors are placed 0.015 m apart, centre-to-centre, leaving < 2 mm of sand between each sensor, for a total centre-to-centre array length of 0.12 m. First shot point is 0.03 m east of sensor array, and each subsequent shot location is moved  $0.12 \pm 0.005$  m for a total of eight shot points (asterisks) with a maximum offset of 1.03 m. Location errors are estimated at 10% of numbers shown.

$$Q = \frac{2\pi}{1 - e^{-2\alpha\lambda}}, \quad (3)$$

where  $\lambda$  is the wavelength. At low loss ( $Q \gg 1$ ), the quality factor is more conveniently related to the attenuation parameter (Knopoff 1964), as follows:

$$Q = \frac{\pi f}{\alpha V} = \frac{\pi ft}{\alpha x}, \quad (4)$$

where  $f$  is frequency,  $V$  is the phase velocity, and  $t$  is the time the wave travels.

The use of  $Q$  is advantageous because it is intrinsic to existing seismic datasets and more sensitive to pore–constituents than seismic velocity (Winkler and Nur 1982). Empirical  $Q$  measurements can also verify existing poro-viscoelastic models for attenuation (e.g., Biot 1956; Pham *et al.* 2002). Moreover,  $Q$  estimations are advantageous because this inelastic behaviour of materials to wave propagation may aid in distinguishing between different soil types and help interpretations by confirming degrees of soil saturation. Departures in measured  $Q$  from expected  $Q$  values that are the result of only saturation changes ( $Q_{dry} \geq Q \geq Q_{wet}$ ) may be useful to detect unexpected changes in

local effective stress, such as caused by over-pressured strata, leaky pipes, etc. (Petak and Atkisson 1982), which may increase or decrease  $Q$  (Pham *et al.* 2002) outside the range of expected values. A change in lithology may also increase or decrease  $Q$  because different materials exhibit different  $Q$  values, e.g., lab values show  $Q$  of 21 in sandstone and 45 in oolitic limestone (Knopoff 1964).

Although small strain ( $< 10^{-7}$ ) attenuation mechanisms can be considered to be linear (Knopoff 1964), they are nevertheless dependent on both stress and water saturation (Biot 1956; Pham *et al.* 2002). Prior laboratory experimental techniques are not yet fully transferrable to the field, but their results show general expected *in situ* relationships between  $Q$ , water saturation, and stress.

Although  $Q$  appears to have overall lower values in unconsolidated sediments, different rock types (Winkler and Nur 1982; Cadoret *et al.* 1998), as well as unconsolidated sediments (Barrière *et al.* 2012), show similar trends in  $Q$  with water saturation and stress.  $Q$  is largest in dry conditions, reaches a minimum at partial saturation, and increases again approaching full saturation (Murphy III 1982).  $Q$  is sensitive to water saturation because

of attenuation from local fluid flow, which reaches a maximum at partial saturation (Biot 1956; Pride and Berryman 2003). In general, larger stresses increase  $Q$  as grain contacts become more elastic (e.g., matrix elasticity  $\propto$  stress<sup>1/3</sup> (Mindlin 1949) and attenuation from internal friction between grains decreases (Pham *et al.* 2002).  $Q$  is frequency independent in dry conditions, but frequency dependent where wet (Winkler 1985); nevertheless, the small change in  $Q$  (< 5%) over a substantial frequency range (0.8–70 kHz) (Blair and Spathis 1984) justifies  $Q$ -measurement methods that assume a frequency-independent  $Q$  (e.g., spectral ratio method).

The spectral ratio method (Báth 1974) is commonly used (Tarif and Bourbie 1987; Jongmans 1990) to produce robust, frequency-independent, *in situ*  $Q$  estimates, insensitive to focusing effects (Tonn 1991). Ideally, the method assumes regular spatial sampling of measured amplitudes along the propagation direction. However, in media with large vertical velocity changes, adjacent sensors may receive rays that travel along significantly different raypath lengths. In such cases, the presence of large  $Q$  gradients may vio-

late the assumed equivalency of  $Q$  between the ray paths of the reference and measured signals and can lead to false  $Q$  estimates—e.g., negative values of  $Q$ —and is a common problem in the near surface for both surface seismic and Vertical Seismic Profiling (VSP) investigations (Haase and Stewart 2006; Raikes and White 2006). For these cases, we compensate by considering the average  $Q$  along the estimated ray paths. Many other techniques (Engelhard 1996; Raikes and White 2006) also suffer from the traditional assumption of the spectral ratio method.

A well-documented and publicly available seismic dataset (Lorenzo *et al.* 2013), collected in a mid-sized, two-layered sand tank (~6 m × 9 m × 0.44 m), is useful for the open evaluation of the relationship between *in situ*  $Q$ , water saturation, and stress and because it is collected with a field-scalable methodology (Figure 1; Table 1). The sand tank contains well-sorted, medium-grained sand.

The data were acquired as eight experimental seismic datasets (e.g., Figure 2), each in the same sand tank at a specific water table level (WL1 through 8) (Table 2). In this experiment, each

**Table 1** Source and sensor equipment and software requirements and seismic acquisition parameters, adapted from Lorenzo *et al.* (2013).

<b>Seismic sensor</b>	
Sensor characteristics	Piezo-electric accelerometer of polyvinylidene fluoride film composition (ACH-01 from Measurement Specialties Inc.); nominally flat response of ~9 mV/g ± 1 mV, response over 20–20 kHz frequency range.
Stage 1 signal conditioning	100-fold operational amplifier (LT1115 from Linear Technologies)
Stage 2 signal conditioning	10-fold audio amplifier, (DI800, from Behringer) converts single-ended signal to differential. Output low impedance (680 Ω), matches required input impedance for analog-to-digital acquisition (AD) card.
Pseudo-array dimensions	64 sensors, 0.03–0.87 m source–receiver offsets, ~0.017 m sensor spacing (Figure 1)
<b>Recording electronics</b>	
Multi-purpose digital acquisition card	Onboard, Peripheral Component Interconnect (PCI)-based AD card with an eight-differential channel mode input (Model PCI-6251 from National Instruments, Inc.), software triggering, and low-impedance analog output for source wavelet.
Instrument control software	Modified version of Multi-Function-Synch AI-AO.vi written in “G,” a commercial virtual instrument software programming language (from National Instruments).
Sample rate	72 kS/s, per analog input differential channel (8)—maximum possible of 156.25 kS/s.
Nyquist frequency	36 kHz
Input and output voltage resolution	1 in 16 bits; 305 mV (+ 5%) for a ± 10V range.
Acquisition format	LabView© (National Instruments) ASCII format converted to SEG-Y (Barry <i>et al.</i> 1975) using <i>seg2seg</i> (Sioseis 2011). SEG-Y data records for each sensor have 13 μs sample intervals and contain 780 samples.
<b>Seismic source</b>	
Source wavelet	Ricker wavelet, central frequency at 10 kHz, 23 samples at 50 kS/s, 50 ms wide side lobes; synthesised digitally by PCI-6251 AD card.
Seismic source generator	Magnetostrictive ultrasonic transducer (Model CU-18 from Etrema Products Inc.). Low-impedance audio amplifier (Model RMX 2450 from QSC Audio Products LLC) amplifies input Ricker source wavelet to drive this transducer at +150 V (max.); Shots (eight) are spaced ~ 0.0017 m apart (Figure 1).
Seismic software filtering, manipulation and display	Seismic Unix Processing System (Stockwell 1999).

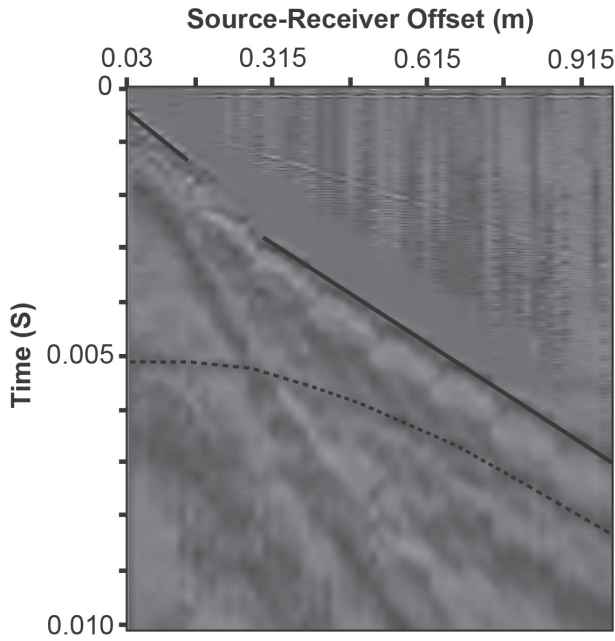


**Figure 2** Representative time versus offset pseudo-walkaway gather for seismic data collected in a 0.44-m-thick sand, which overlays cement. For all experiments, eight receivers were placed linearly with 0.015 ( $\pm 0.005$ ) m spacing. Each gather consisted of eight shots with a 0.03m nearest offset for the first shot and an additional 0.12 m for each subsequent shot (0.03–0.975 m source–receiver offset) (Lorenzo *et al.* 2013). Traces are gain corrected using 0.5 s windowed Automatic Gain Control (AGC) for plotting purposes but not for analytical methods. A continuous refraction through the sand (solid black line) and a reflection from the top of the cement below the sand (dashed black line) are used to constrain velocity models (Figure 11).

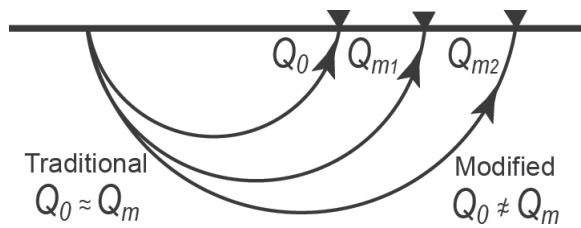


**Figure 3** Traditional spectral ratio method assumes that the reference  $Q$  ( $Q_0$ ) is similar along different trajectories. In our modified method, we use  $Q_0 \sim 4$  (equation (6)) and avoid non-physical results, such as  $Q < 0$ .

of the eight accelerometers were kept far enough away from the edges of the tank so as to maintain a constant stress as water level varied. Sensors were buried 1 cm below the sand surface to improve coupling (Figure 1). The pseudo-walkaway acquisition geometry (Vincent *et al.* 2005) used a fixed array of eight accelerometers (Table 1) and eight off-end, shot point gathers (Figure 2) collinearly transposed (Evans 1997). In order to be certain that slightly different calibration constants between sensors do not affect our analysis, the pseudo-walkaway geometry allows us to go reorganise the data according to a common receiver for different shot offsets. Nominally, a shot point spac-

ing equal to the geophone spread length provided laterally continuous, but non-overlapping, subsurface seismic returns while expediting data acquisition. Small static shifts between sub-arrays exist only if there are lateral subsurface heterogeneities.

These data advantageously sample seismic attenuation effects over a range of theoretically estimated effective water saturation (0–1) and total effective stress (0–5000 Pa) but derived only from the unconfined sediment column. A minimum of 3 hours between data collection and imbibition allowed enough time for the water table to reach equilibrium in the medium-grained sand (Gillham 1984).  $Q$  measurements should be simpler to interpret in the imbibition case because less patchy saturation is expected (Toms, Müller and Gurevich 2007). Seismic source-to-receiver offsets range from 0.03 to 0.975 m, and the sensor spacing is 0.015 m. Prominent continuously refracted seismic arrivals are preferable for estimating  $Q$  with depth because they ideally sample a range of depths in the sand body. For the case of a gradient-velocity layer, refracted first arrivals received at greater source–receiver offsets represent continuously refracted rays, which are turned from increasingly greater depths (Aki and Richards 1980).

We employ a modified spectral ratio method to estimate *in situ*  $Q$  because of the large  $Q$  gradient in shallow, unconsolidated sand. We estimate interval  $Q$  values from average raypath  $Q$  values, penetration depths, and travel times. We expect observable relationships between *in situ*  $Q$ , stress, and water saturation similar to previous core sample resonance studies, which could lead to a seismic attenuation constraint on these parameters in the field.

## METHODS AND THEORY (A THROUGH D)

### Modified spectral ratio method

Both the modified and unmodified spectral ratio methods (Figure 3) estimate *in situ*  $Q$  through a ratio of measurements taken at sensors that share a common source but are located at different distances from the common source (equation (1)). To solve for  $Q$  (equation (4)), these ratios are graphically displayed in a semi-log plot versus frequency and interpreted with a best-fitting line (Figure 4). A chosen wavelet and its amplitude spectra serve as a reference signal ( $A_0$ , equation (1)) and the slope ( $m$ ) of a best-fitting line to these results is an estimate of  $Q$  for the propagating media.

$$m = \frac{\pi t_0}{Q_{eff}} - \frac{\pi t_m}{Q_{eff}}, \quad (5)$$

where  $t_0$  and  $t_m$  are the travel times ( $t_m > t_0$ ) to a reference and measured location, respectively, and  $Q_{eff}$  is the effective  $Q$  obtained by an unmodified (traditional) spectral method.

We modify the traditional spectral ratio method by assuming that a wave arriving at a reference location samples a markedly different  $Q$  ( $Q_0$ ) than at the measurement location ( $Q_m$ ), so that the slope ( $m$ ) can be viewed as follows:

$$m = \frac{\pi t_0}{Q_0} - \frac{\pi t_m}{Q_m}. \quad (6)$$

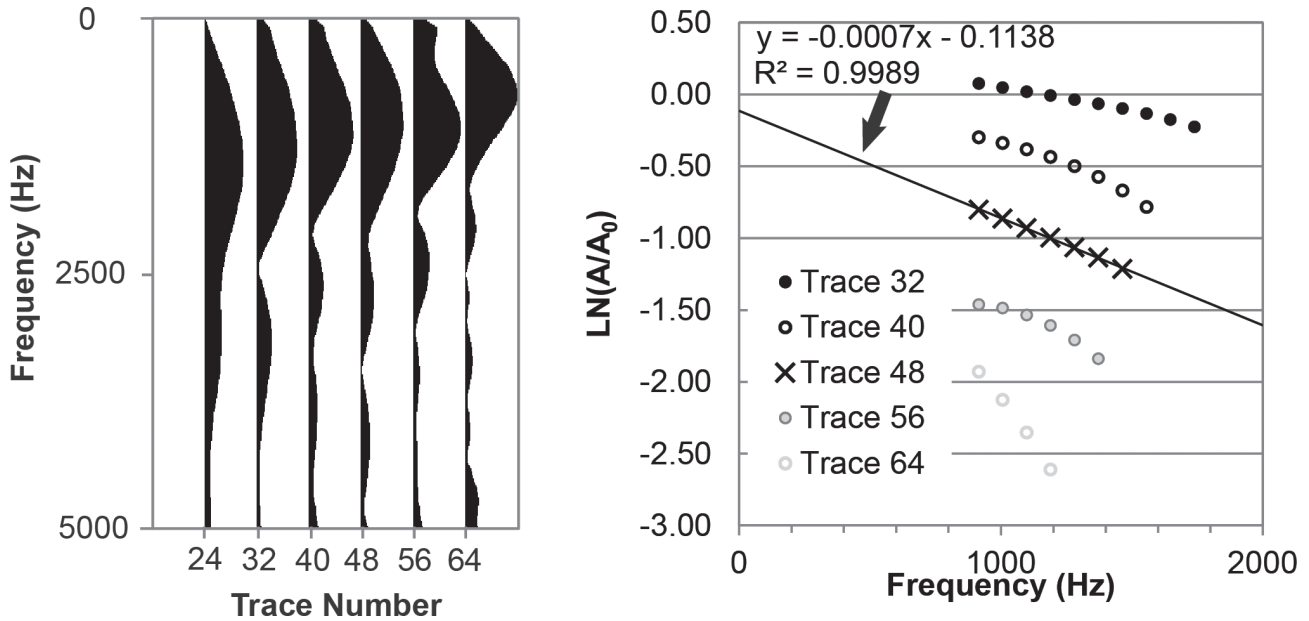


**Figure 4** (A) Example unfiltered amplitude spectra from six extracted wavelets (Lorenzo *et al.* 2013) from a continuous refracted event arising from a water table at 0.14-m depth (WL5; Table 1) at different source–receiver distances. We note that for a pseudo-walkaway layout (Lorenzo *et al.* 2013), one physical sensor can be used to receive seismic arrivals at different shot-to-receiver offsets (i.e., different trace numbers). The leftmost trace (#24) is used as the reference for estimating  $Q$ . Spectral ratio calculations are confined to frequencies of the measured wavelet neighbouring the peak frequency and whose amplitudes are  $> 30\%$  peak frequency. Separation between each eighth trace shown is 0.12 m (Figure 1). (B)  $Q$  is estimated from the slope of the least-squares, best-fit line to the measured spectral ratios at each frequency—we show only one case for clarity. We emphasise that data collected by the same receiver removes calibration effects that could cause errors if different receivers are used. Each of the five common-receiver groups uses the same receiver but may contain different numbers of traces because we select only lowest noise wavelets. Each group is interpreted to represent a different depth in the sand body. We use wavelets of refraction events received at distances larger than several wavelengths from the source ( $\sim 0.3$  m) because they show fewer near-field effects (Haase and Stewart 2010) and less interference from surface waves.

For example, in those cases where we find that  $Q_{eff} < 0$ , which does not appear to be physically meaningful, this approach produces a positive slope ( $m > 0$ ), is more simply interpreted as  $Q_m > Q_o$ .

For an estimation of  $Q_m$  (equation (6)), we need  $Q_o$ ,  $t_o$ , and  $t_m$ . We assume  $Q_o = 4$ , based on previously measured attenuation parameters in partially saturated, unconsolidated sand (20 cm thick) (Oelze, O’Brien and Darmody 2002). Travel times ( $t_o$  and  $t_m$ ) are more consistently picked at the peak amplitude of the wavelets. We use the peak amplitude time, representative of the frequency-independent group velocity, because frequency-dependent travel times and their phase velocities are often difficult to distinguish in seismic data (Futterman 1962).

Discrete sections of the waveform are sampled for spectral ratio calculation (Figure 4). Wavelets received at distances larger than several wavelengths from the source ( $\sim 0.3$  m) show fewer near-field effects (Haase and Stewart 2010) and less interference from surface waves. In order to increase accuracy of  $Q_m$  estimates, we confine spectral ratio calculation to frequencies neighbouring the peak frequency and whose amplitudes are  $> 30\%$  peak frequency—this procedure avoids regions of the spectrum that can be more heavily influenced by spectral interference and other noise (Reine, van der Baan and Clark 2009).

In order to remove the effects of possible variable bandwidth sensitivity (Mateeva 2003), each  $Q_m$  value is calculated from spectral ratios with common receivers between the eight receivers (Figure 5). Otherwise, bandwidth sensitivity could remain an issue by influencing the slope ( $m$ ) of the spectral ratios for different receivers, allowing larger variations in measured  $Q$  values ( $\pm 0.9$ ) than indicated by presented errors (cf.  $\pm 0.1$ ).

### $Q$ and the attenuation parameter ( $\alpha$ ) in highly attenuating media

For comparison with the results of other workers (e.g., Badri and Mooney 1987; Jongmans 1990; Barrière *et al.* 2012), herein, we

continue to use the low-loss approximation  $Q \approx \frac{\pi f}{\alpha V}$  (equation (7)) (Futterman 1962) to relate  $Q$  to the attenuation parameter ( $\alpha$ ), which incurs at least a 10% difference ( $Q < 30$ ) in contrast to the exact Futterman (1962) solution, as follows:

$$Q = \frac{2\pi}{1 - e^{-\frac{2\alpha V}{f}}} \quad (8)$$

where  $V$  is phase velocity and  $f$  is frequency.

**Table 2** Water table (WL1-8) from public dataset (Lorenzo *et al.* 2013) and their depths with respect to the top of the sand body, which is 0.44 m thick.

Water table level	Depth (m) ( $\pm 0.02$ )
WL1	0.34
WL2	0.29
WL3	0.24
WL4	0.19
WL5	0.14
WL6	0.07
WL7	0.05
WL8	0.01

For each water table depth, eight shots were performed in a pseudo-walkaway seismic gather, increasing shot–receiver offset by 12 cm after each shot. Hardware settings: 0.5-s record length, 12.5- $\mu$ s sample interval, 8 geophones, 1.5-cm geophone spacing, and 3-cm smallest shot–receiver offset (Lorenzo *et al.* 2013).

### Changes in water saturation and stress with depth

At any given depth in the sand tank, both water saturation and stress (Figure 6) vary with the location of the water table (WL1 through 8) (Table 2). Understanding these effects can help interpret the variations of  $Q$  versus depth. We calculate water saturation and stress using the physical properties of sand (Table 3) and soil water characteristic curves (SWCC) (Shen *et al.* 2016).

In the absence of *in situ* saturation measurements, SWCC are used to calculate water saturation with depth above a given water table. We use the method of van Genuchten (1980) to fit capillary pressures and water saturations empirically for a sand similar to that in our experiment (Table 3).

$$S_e = \frac{\theta - \theta_r}{\theta_s - \theta_r} = \left[ \frac{1}{1 + [\alpha(u_a - u_w)]^n} \right]^{\frac{n-1}{n}}, \quad (9)$$

Model parameters	Sand	Reference
Sand grain density (kg/m <sup>3</sup> )	2650	
Pore water density (kg/m <sup>3</sup> )	1000	
Pore air density (kg/m <sup>3</sup> )	1.22	(Mavko <i>et al.</i> 2005)
Gravitational acceleration (m/s <sup>2</sup> )	9.81	
Sand porosity	0.40	(Beard and Weyl 1973)
van Genuchten $n$ fitting parameter	5.69	
van Genuchten $\alpha$ fitting parameter	4.56	(Engel <i>et al.</i> 2005)
Irreducible water content	0.024	
Saturated water content	0.38	
Matrix cohesion (Pa)	300	(Krantz 1991)

Fitting parameters are calibrated for capillary pressures in psi. Seismic data velocity models do not exceed 200 m/s (Lorenzo *et al.* 2013). To explain these low velocities, a Biot–Gassmann (Gassmann 1951) poroelastic model implies a water saturation  $< 1$ . A saturated water content of 0.38 is reasonably consistent with this assumption.

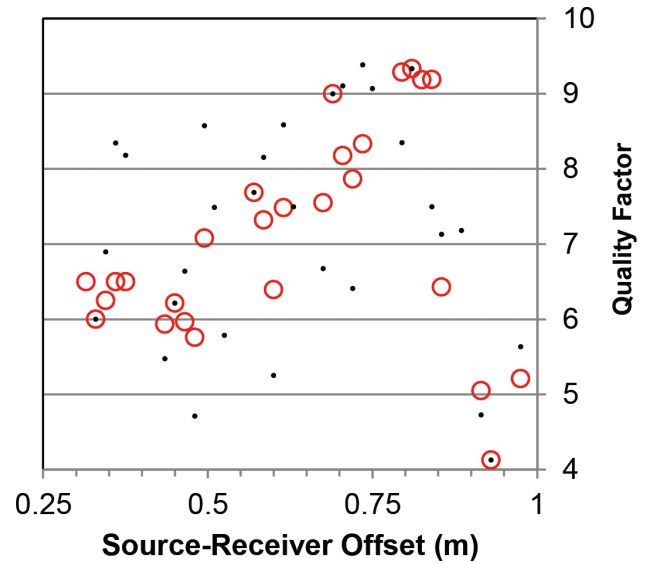


**Figure 5** Comparison of  $Q_m$  values measured with a common reference receiver (red unfilled circles) show less variability than if receivers use different references (black filled circles) probably because of slightly different bandwidth sensitivities between sensors.

where  $S_e$  is effective saturation;  $\theta$  is the volumetric water content;  $\theta_r$  is the residual water content;  $\theta_s$  is the saturated water content, which is equivalent to porosity;  $\alpha$  and  $n$  are van Genuchten (1980) empirical fitting parameters; and  $(u_a - u_w)$  is the capillary pressure (Table 3). An SWCC can be converted into a pressure head–water saturation profile that is consistent with natural water saturation profiles (Desbarats 1995). We can solve the above equation for capillary pressure  $(u_a - u_w)$  and set it equal to the weight of the water column supported above the water table (pore pressure equation).

Following Shen *et al.* (2016), we determine the effective average stress ( $P$ ) at grain contacts as follows:

$$P = (\sigma_t - u_{pore}) + \sigma'_s + \sigma_{co}, \quad (10)$$

**Table 3** Porosity and fitting parameters are measured in a similar medium-grained sand, 0.35 mm (Engel *et al.* 2005) compared with a 0.38-mm mean grain size (Lorenzo *et al.* 2013).

from the sum of net overburden stress ( $\sigma_t - u_{pore}$ ) and interparticle stress ( $\alpha \sigma'_s + \sigma_{co}$ , where  $\sigma_t$  is the weight of the sediment column (Terzaghi, Peck and Mesri 1996),  $u_{pore}$  is pore pressure,  $\sigma'_s$  is soil suction stress, and  $\sigma_{co}$  is apparent tensile stress at the saturated state caused by cohesive or physicochemical forces (Bishop 1960).

Soil suction stress (equation (11)) is then derived from Van Genuchten's fitting parameters for SWCC (Song *et al.* 2012).

$$\sigma'_s = -\frac{S_e}{\alpha} \left( S_e^{\frac{n}{1-n}} - 1 \right)^{\frac{1}{n}} \quad (11)$$

**Interval Q**

To ensure monitoring of local changes in  $Q$  and not only the average  $Q$  over the entire ray path, we estimate  $Q$  within depth intervals ( $Q_{int}$ ). Assuming we have a sequence of horizontal layers with separate rays turning at the top and the bottom of each layer, as follows:

$$Q_{int} = \frac{t_n}{\frac{T_n}{Q_n} - \frac{(T_n - t_n)}{Q_{n-1}}} \quad (12)$$

where  $Q_{int}$  and  $t_n$  are measured within each layer ( $n$ ) and where the travel time ( $T$ ) and  $Q$  are measured along entire ray paths to the top ( $T_{n-1}$  and  $Q_{n-1}$ ) and bottom ( $T_n$  and  $Q_n$ ) of the layer (Tonn 1991).

Values of  $Q_{int}$  are more influenced by the properties of those parts of the ray path where most time is spent. In the case of our

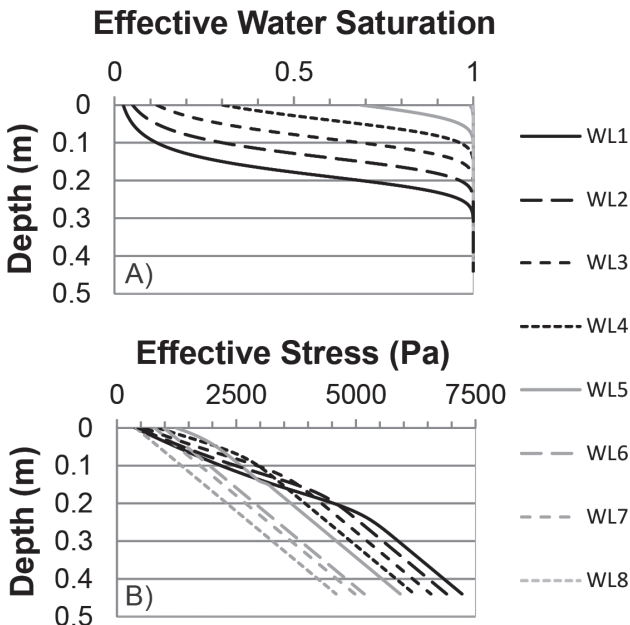


**Figure 6** As the water table rises (WL1-8), calculations indicate that water saturation above the water table increases, whereas below the water table, stresses decrease as the effective weight of the sediment column decreases.

interpreted velocity–depth models (Figure 7), we calculate how much time along the ray path is spent within each layer and find that, for the deeper few centimetres of the sand, this can be as much as > 35%. For this reason, we opt to assign the estimated  $Q_m$  to the bottom of each interpreted layer ( $\pm 10^{-2}$  m). Linear best-fits of the  $Q$  values themselves help characterise the overall change ( $dQ/dz$ ) and linear dependence ( $r$ ) of  $Q_{int}$  with depth and can be used to understand and represent how changes in water saturation and stress may affect  $Q$  (Figure 8).

In order to determine  $t_n$ , ray paths and their travel times to each of the receivers are calculated (Slotnick 1936; Cerveny 2005) from velocity–depth profiles. Forward modelling by trial-and-error ray uses constant velocity and gradient velocity layers (Figure 7) and matches the principal refracted first arrivals ( $\pm 10^{-4}$  s) and reflected arrivals. Lateral homogeneity is assumed where a resultant, simple, one-dimensional velocity–depth model represents the average structure over the range of source–receiver offsets. In order to calculate the time spent by different rays in each layer, we first calculate more ray paths than needed but select only those that surface nearest to actual receiver locations ( $\pm 10^{-3}$  m).

**RESULTS**

The relationship between water saturation and  $Q_{int}$  (Figure 8) may be more evident when examined at a particular depth, as the minimal stress change effectively isolates the influence of water saturation. The increase in attenuation ( $1/Q_{int}$ ) (Figure 10) at partial saturation (WL2-4) and its decrease, either under relatively dry conditions (WL1) or nearly saturated conditions (WL5), seem consistent with a previously published poro-viscoelastic model for seismic attenuation (Barrière *et al.* 2012) in sand where the attenuation from local fluid flow is predicted to peak at maximum relative permeability (~60% water saturation) of the pore constituents.

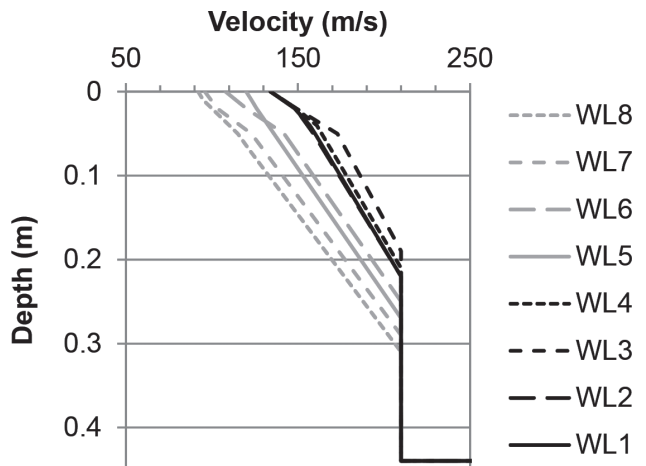


**Figure 7** Best-fitting travel time calculations ( $\pm 10^{-4}$  s) to raw data (Figure 2) obtained via ray tracing are used to generate velocity–depth profiles. These velocity models are necessary to calculate interval  $Q$  values along with the maximum penetration depths of each ray path.

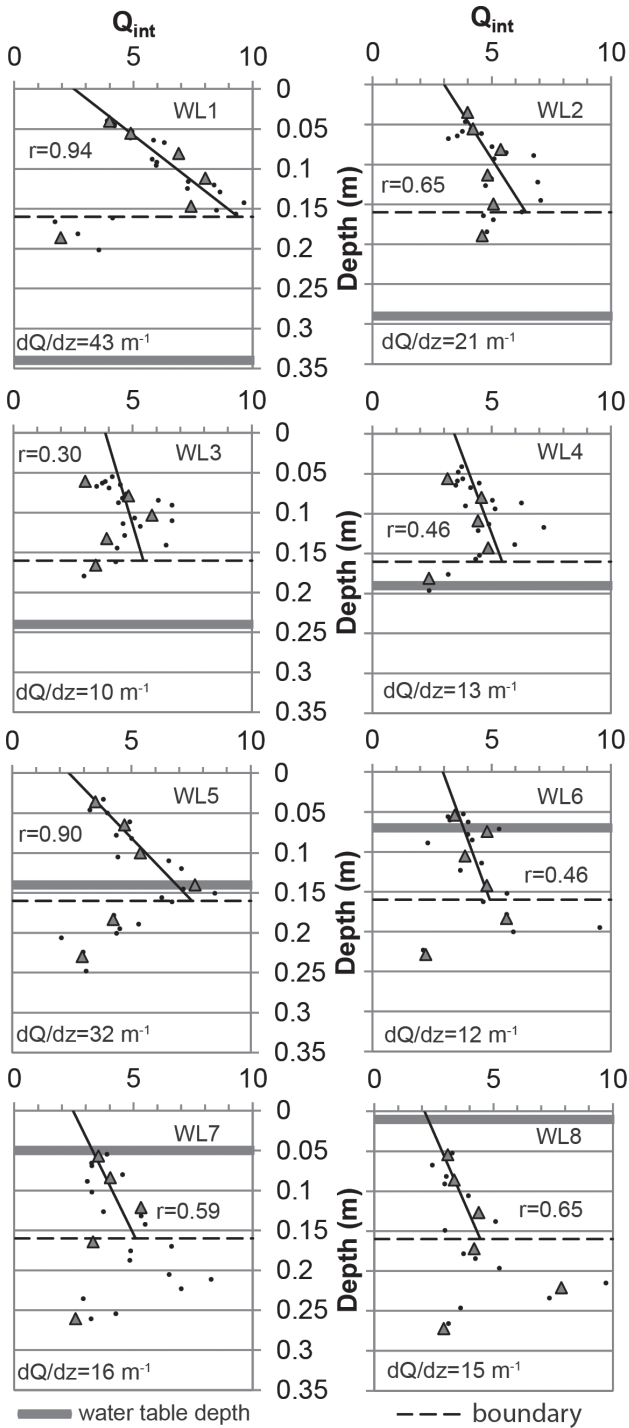


**Figure 8** As an aid to the interpretation of the diagrams, we can subdivide the sand body into a “drier” region, above the dashed line. The largest  $Q$  gradient ( $dQ/dz$ , solid line) appears within the dry region (WL1). Under low saturation conditions (~dry), increases in  $Q_{int}$  with depth likely result primarily from increases in stress. As the water table rises (WL2-WL8; thick, gray lines), the changes in linearly fitted  $dQ/dz$  ( $10 \text{ m}^{-1}$  to  $43 \text{ m}^{-1}$ ) result from the complicated relationships between  $Q$ , stress, and water saturation.  $Q$  estimates obtained using a common receiver (gray triangles) are useful (Figure 2) because they show lower  $Q$  variability.

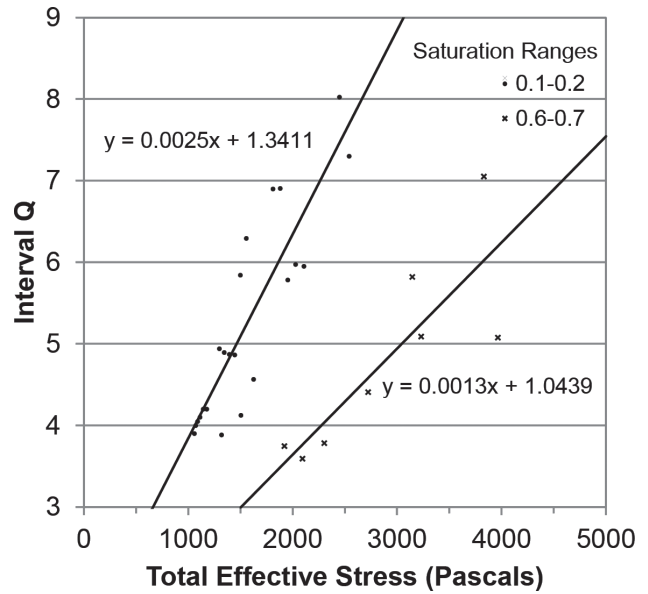


**Figure 9** Representative  $Q$ -stress ( $\sigma$ ) distribution over two constant ranges of water saturation (0.1–0.2 and 0.6–0.7) can be approximated linearly. In our experimental data, stresses are expected to range from 0 to 5000 Pa.

Concurrent changes of water saturation and stress both affect  $Q_{int}$  (Figures 8 and 9) but help complement previously published results (e.g., Hamilton 1976; Murphy III 1982), which only consider  $Q$  variations with each parameter, individually. We measure changes in  $dQ/dz$  (Figure 8) over a large range of theoretically estimated effective water saturation (0–1). A strong linear dependence appears to exist between  $dQ/dz$  for both relatively dry conditions ( $r > 0.94$ ) and relatively wet conditions below the water table ( $r > 0.90$ ); otherwise, the dependence is weak ( $r < 0.46$ ). In dry conditions, the calculated water saturation has values of  $\sim 0.1$ – $0.2$ , and in wet conditions, the water saturation is calculated at  $0.6$ – $0.7$ . The highest value ( $43 \text{ m}^{-1}$ ) for  $dQ/dz$  occurs under dry conditions and the lowest ( $10 \text{ m}^{-1}$ ) under wet conditions.

With regard to relationships between  $Q$  and stress (Figure 9), our analysis shows that over a small range of calculated saturation ( $\pm 5\%$ )  $Q_{int}$  and stress ( $\sigma$ ), a linear correlation can be used to characterise the trends. For example, under dry conditions,  $dQ/d\sigma = 0.0025/\text{Pa}$ , ( $r > 0.77$ ) and where water saturation is higher  $dQ/d\sigma = 0.0013/\text{Pa}$  ( $r > 0.7$ ). Furthermore, the maximum  $Q_{int}$  value occurs under dry conditions and the minimum  $Q_{int}$  under wetter conditions (Figures 8, 9 and 10).

An interesting minor note is that, in our unconsolidated sand case, the relationship between these extreme values can be approximated empirically as  $Q_{dry} \approx Q_{wet}^{1.4}$  when an exponential relationship is assumed. We used the minimum  $Q$  values at each depth to determine the best-fitting curve. Re-analysis of previous work (Winkler and Nur 1982) that collected  $Q$  from sandstone samples also reveals an analogous relationship between  $Q_{dry}$  (water saturation = 0) and  $Q_{wet}$  (water saturation = 0.9), where

$Q_{dry} \approx Q_{wet}^{1.8}$ . We consider that the smaller value of the exponent taken from the analyses (1.4 cf. 1.8) for our sand case may likely be the result of smaller friction between the unconsolidated grains. Mindlin (1949) theory would support that the shallower (and drier) sand would be under less stress, and as a result, the attenuation caused by internal friction between grains would decrease as well (Pham *et al.* 2002).

**DISCUSSION**

Whereas the modified spectral ratio may help handle cases of large subsurface heterogeneity, the assumption of a different reference  $Q$  ( $Q_0$ ) also has the potential to introduce additional error. Because we expect that the  $Q$  heterogeneity is more detectable in lab-scale experiments of soils when also  $Q$  values are low in general, we partly evaluate the effect of this assumption by testing a nominal range of  $Q_0$  values (1–10 for the loose soil conditions of this particular experiment. A measure of the sensitivity of  $Q$  values, with respect to the original  $Q_0$  used, can be estimated through consideration of a typical seismogram (Figure 2) and its analysis (Figure 9). For this case, we consider a uniform random distribution of values within the range of possible values for velocity (150 m/s  $\pm$  15), best-fit spectral slope value (0.006  $\pm$  0.0001 m) and  $Q_0$  (1–10). In summary, an order

of magnitude change in the  $Q_0$  appears to also change individual  $Q_m$  equally as much. In a worst-case scenario, in a lesser but still significant way, variations in estimated slope and velocity (distance/time) also affect the final result if an unusually large reference  $Q_0$  is chosen. In comparison to other results that may use the modified spectral method, we recommend common low value ( $Q_0 \sim 4$ ) where the estimated  $Q_m$  is not as sensitive. For the given value of  $Q_0$  (4) in this paper, we expect that significant trends interpreted in the relationships between  $Q$  with water saturation and stress remain unaffected.  $Q$  would still increase with stress and reach a minimum at partial saturation.

Nevertheless, our estimations of  $Q$  based on an assumption of  $Q_0$  yield a range of  $Q_m$  values, which are consistent with other studies (Figure 14) in unconsolidated sand and agricultural soil for comparable stresses and saturations. For example, Oelze *et al.* (2002) and Barrière *et al.* (2012) also derive well-behaved spectral ratios (correlation coefficient:  $r > 0.95$ ). They determine that in an adequate number of frequency samples ( $n > 3$ ), and even after several iterations of  $Q_m$  measurement,  $Q_m$  estimates appear to remain comparable ( $\pm 10^{-1}$ ). Based on the least-squares, best-line fitting (e.g., Figure 4B), our results are also well behaved ( $\pm 10^{-1}$ ). We note that we use more frequency samples ( $n > 4$ ) and that, for our continuous wavelets, any further points fall on the line through the original points. The small correlation error is small and accounts for the random fluctuations, although these real and important biases can arise from apparent attenuation.

We note that we include the low-loss approximation (Futterman 1962) to explain the relationship between  $Q$  and the

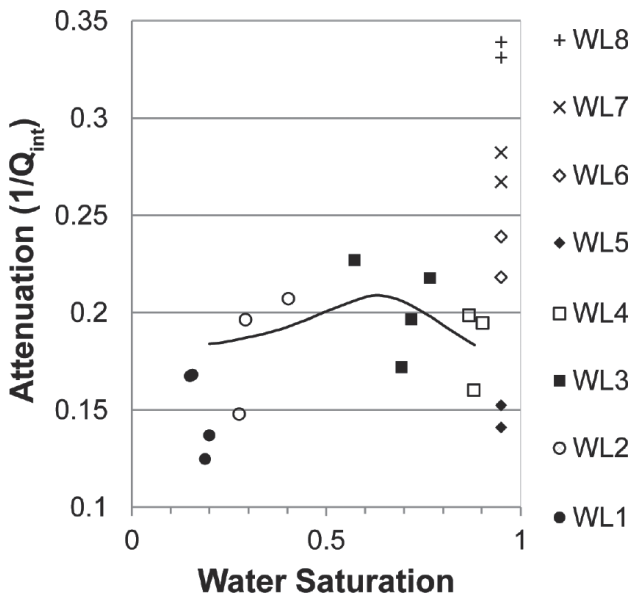


**Figure 10** Above the water table (WL1-5), the distribution of attenuation–water saturation values estimated at 0.1 m ( $\pm 0.01$ ) depth (Figures 6(A) and 8) are consistent with a best-fit poro-viscoelastic model (i.e., Biot theory) based upon attenuation measurements during imbibition in sand at a similar depth (0.17 m) (Barrière *et al.* 2012). We also show those cases for when the water table rises above 0.1 m (WL6-8)—here, attenuation increases progressively. We interpret that this behaviour may be the result of changes in the grain size at about this level between the two different layers (Lorenzo *et al.* 2013) of sand and perhaps an unusual amount of residual air, not expected in a homogeneous model, decreasing the total effective stress.

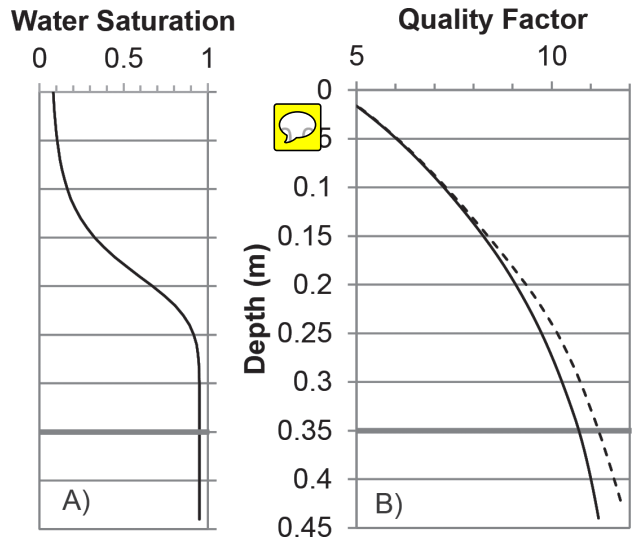


**Figure 11** Potential seismic constraint on water saturation in sand is consistent with previously shown relationships between  $Q_{int}$ , stress, and water saturation (Figures 8–10). Based upon (A) a typical water saturation profile for sand with a water table depth of 0.34 m (e.g., WL1), (B) the expected response (dashed line) is bound maximally by  $dQ/dz$  observed for mostly dry sand (Figure 8, WL1) and minimally by  $Q_{dry}^{0.71}$  (solid lines)

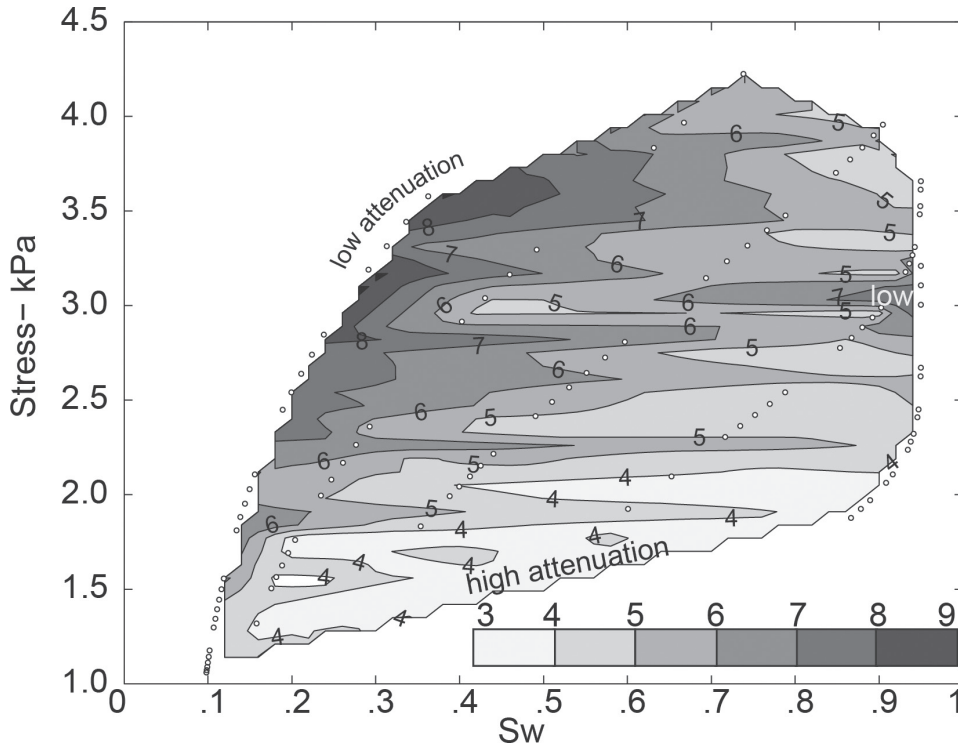


**Figure 12** Interval quality factors, which are derived via a modified spectral analysis method of seismic data are plotted against theoretically derived effective stress and saturation. As water levels rise in the sand body during the experiment, data points plot more to the right (101 black dots). Shaded contour intervals generally indicate shallower/drier (darker) and deeper/wetter (lighter) portions of the sand body. At low saturation levels ( $< 0.3$ ) and lower water levels in the experiment, seismic attenuation appears to be lower ( $Q_{int}$  increases) with increased stress (depth and matric suction). However, at higher saturation levels, increase ( $> 0.6-0.7$ ) attenuation appears decoupled from stress changes.

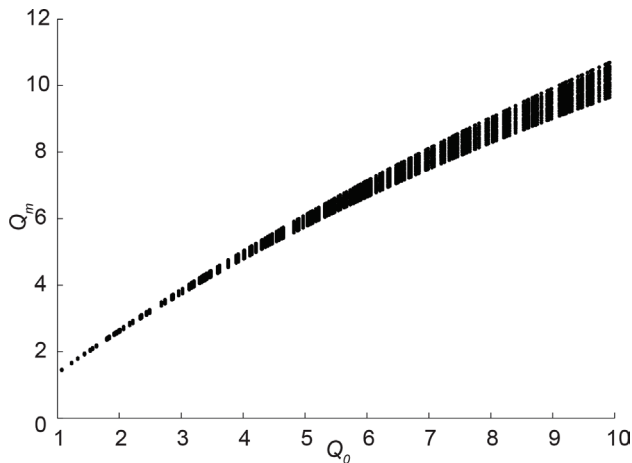


**Figure 13** Sensitivity of calculated  $Q_m$  to a reference  $Q_o$ . A slightly non-linearly relationship exists over a possible range of  $Q_o$  from 1 to 10. In addition, for a given  $Q_o$ , the variation in  $Q_m$  is also sensitive to the local value of  $m$  (equation (5)) and to the time interval over which the frequency amplitude is observed to decay. Spread of  $Q_m$  uses values selected within reasonable ranges for local velocity and  $m$  (e.g., Figures 2 and 4). Calculations employ a finite, uniform, but random, distribution of values within each specified range.

attenuation parameter ( $\alpha$ ) (equation (7)) when deriving the spectral ratio method, although it incurs at least a 10% error in highly attenuating media ( $Q < 30$ ). In addition to keeping  $Q$  estimates comparable to previous studies, the low-loss approximation does not adversely affect the observed  $Q$ -trends with stress and water saturation, which are noticeable in both low- and

high-loss porous media. Moreover, interpretations in high-loss porous media can be inhibited where a strict definition relating  $Q$  to  $\alpha$  is used (equation (8)), because  $Q$  values decrease to an asymptote of  $2\pi$  as  $\alpha$  increases and because changes in  $Q$  become smaller and harder to distinguish. Whereas trends in  $Q$  are still interpretable and increases or decreases in  $Q$  are still related to changes in attenuation, when the low-loss approximation is applied to high-loss conditions, the exact physical meaning of  $Q$  is no longer valid.

Changes in  $Q_{int}$  with depth (Figure 8) can be interpreted from established relationships between  $Q$  and either water saturation or stress. We detect an increase in  $Q_{int}$  with predicted stress (Figure 9), and Pham *et al.* (2002) also note that elastic moduli can increase concomitantly with  $Q$  in response to an increase in differential pressure. Because stress and water saturation both increase with depth, it is not immediately clear whether we should expect a positive or negative  $dQ/dz$ . Based on the expected saturation values over our depth ranges (e.g., Figure 5), we interpret that the common, positive  $dQ/dz$  values (Figure 8) result from an increase of stress and greater internal friction between grains (Pham *et al.* 2002), which leads to less attenuation (higher  $Q$ ). In contrast, an increase in local fluid flow (Biot 1956) at higher relative permeability would increase the attenuation. Although  $dQ/dz$  may remain positive for every water level ( $10-43 \text{ m}^{-1}$ , Figure 8), partially saturated sand also displays the smallest values of  $dQ/dz$  and  $dQ/d\sigma$ —e.g.,  $10 \text{ m}^{-1}$  (Figure 8), where saturation ranges from 0.3 to 0.7 (Figure 9), and  $0.0013/\text{Pa}$ , where saturation ranges from 0.6 to 0.7 (Figure 9). These trends support an interpretation that minimal  $Q_{int}$  values (highest

attenuation values) occur at partial saturation (0.6–0.7 in unconsolidated sand) for any given depth or stress and most likely result from local fluid flow reaching a maximum (Biot 1956; Barrière *et al.* 2012).

For four of the water-level cases (WL6-8) in this public dataset, we document a small  $dQ/dz$  (Figure 8) below the water table, likely resulting from a decrease in the effective stress gradient (Figure 6). Where the sediment column displaces water, its effective weight is decreased (Turner 1979), generating less stress at each depth. Because  $Q_{int}$  varies with stress, a reduced stress gradient causes  $Q_{int}$  to increase less with depth. Because  $Q_{int}$  varies with stress, a reduced stress gradient causes  $Q_{int}$  to increase less with depth. Below the water table, a  $Q_{int}$  decrease with stress is evident (Figure 8) where it is evaluated at any particular depth after the water table rises and effective stress decreases in the saturated sand. For example, at a water table depth of 0.07 m (WL6), we calculate a stress of  $\sim 1900$  Pa (e.g., Figure 6) and derive a  $Q_{int}$  of  $\sim 4$  in our sand (0.1 m, Figure 8). However, after the water table rises to 0.01 m, we calculate that stress decreases to  $\sim 1300$  Pa, whereas  $Q_{int}$  is seen to decrease to  $\sim 3$  (Figure 10, WL6-8). Whether stress (Hamilton 1976) or water saturation (Murphy III 1982) is more influential on  $Q$  is often debated; however, the dependence of  $Q$  on both water saturation and stress emphasises the importance of each parameter.

Our current results highlight relationships between  $Q_{int}$  values, water saturation, and stress that may be used to place constraints on water saturation with depth, at least for homogeneous, porous media (Figures 11 and 12). In dry sand, because we consider that there is no additional attenuation from local fluid flow,  $dQ/dz$  appears to be largest ( $43 \text{ m}^{-1}$ , Figure 8), and  $Q_{int}$  is most probably dictated by the relationship between  $Q$  and total effective stress ( $dQ/d\sigma = 0.0025/\text{Pa}$ , Figure 2). From our results (Figure 8),  $Q_{int}$  is largest in dry sand and is expected to vary linearly down to a depth ( $z$ ) of 0.16 m according to the following linear relationship:  $Q_{int} = 43z + 2.5$  (Figure 8, WL1). Under conditions of partial saturation (0.6–0.7, Figure 8),  $Q_{int}$  values are expected to be the smallest and can be approximated by the relationship  $Q_{wet} \approx Q_{dry}^{0.71}$ . Similarly, a previously shown relationship relates maximum and minimum  $Q_{int}$  values (i.e.,  $Q_{dry} \approx Q_{wet}^{1.4}$ ) for our unconsolidated sand.

Based on how both  $dQ/dz$  and  $dQ/d\sigma$  vary with changes in saturation (Figures 8 and 9), it is possible that future field studies

that focus on variations of  $Q$  with stress and water saturation may achieve improved resolution ( $\pm 5\%$ ) field values of saturation from *in situ*  $Q$  measurements.  $Q_{int}$  can be more sensitive to water saturation than seismic velocity (e.g., 45% cf.  $< 10\%$  change at 0.1-m depth, 0.1–0.8 water saturation) and, so, may be more desirable for seismic investigation of these *in situ* relationships.

Our interpretations are limited in part by the theoretical calculations of saturation and related effective stress. Below the water table, we assume full saturation, which for field cases may be a good assumption. However, by comparison to *in situ* saturation measurements of a similar, although homogeneous, sand body (Shen *et al.* 2016), *in situ* saturation never reaches more than 0.6 (Shen *et al.* 2016), which suggests remnant trapped air within the sand. Incomplete saturation explains the estimated velocity models that do not reach acoustic velocity values of sound in water of 1500 m/s at the bottom of the sand body (Figure 2). Under conditions of incomplete saturation, the relationships inferred between  $Q_{int}$ , stress, and saturation (Figure 12) should be normalised to a narrower range of conditions, e.g., stress (0–2500 Pa and 0–0.6  $S_w$ ).

Unusually low  $Q_{int}$  values ( $< Q_{dry}^{0.71}$ ) appear for depths  $> 0.16$  m in our dataset (WL1-5, Figure 8), and that may be explained by an additional attenuation mechanism. This unexpected decrease in  $Q$  occurs at a layer boundary between two sand layers with different mean grain sizes ( $\sim 0.38$  mm cf.  $\sim 0.31$  mm) (Lorenzo *et al.* 2013). If grains of different size mix across the boundary, the expected decrease in effective porosity and permeability (Chilingar 1964) could cause heterogeneous saturation as capillary pressures at the boundary would be larger than in either of the two layers (Brooks and Corey 1964; Fredlund and Xing 1994). Heterogeneous saturation is predicted to result in lower  $Q_{int}$  values as the result of macroscopic (not local) fluid flow (Dutta and Odé 1979; Pride and Berryman 2003), where the patches of saturation are larger than the acoustic wavelength and water immiscibly invades the pore spaces previously occupied by air.

The increase of  $Q_{int}$  with stress (Figure 9) and its expected minimum at partial saturation (Figure 10) is seen in  $Q_{int}$ -depth profiles (Figure 8) and also predicted by poro-viscoelastic models (e.g., Biot theory; Biot 1956); however, the small  $Q_{int}$  values ( $< 10$ ) that we measure have yet to be explained (Barrière *et al.* 2012). In Biot theory, waves that pass through media with large

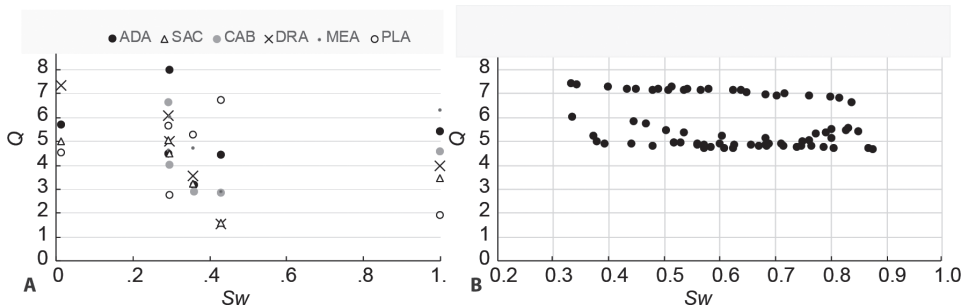


**Figure 14** Examples of  $Q$  in other experiments in loose, porous, granular materials **A** for the case of six agricultural soils (abbreviations—Table 6; Oelze *et al.* 2002) and for **B** uncompacted sand (Barrière *et al.* 2012)

matrix elasticities are predicted to experience less attenuation than waves that pass through media with small matrix elasticities. The current inability to explain these low  $Q_{int}$  values may stem from the characteristically low matrix elasticities of unconsolidated sediments (< 20 MPa), the same problem that makes low seismic velocities (< 200 m/s) (Bachrach, Dvorkin and Nur 1998) difficult to model. An elastic granular contact theory that explains low matrix elasticities of unconsolidated sediments (e.g., extended Walton model; Dutta, Mavko and Mukerji 2010) may potentially be used with a poro-viscoelastic model (e.g., Biot theory) to predict small (< 10) *in situ*  $Q$  values.

In future seismic field investigations, where stress and saturation vary, transfer of our results to the interpretation of the observed attenuation should be carried out with careful consideration of additional factors, including particle shape, sorting, and size. In the controlled experiment we use, the sand is medium grained and well sorted but layered (1.52–1.7 phi average, Lorenzo *et al.* 2013). But if for example, the sorting were poorer, as in many natural systems, then we might expect a reduction in relative permeability. If we agree to accept one of our conclusions that attenuation appears to be greatest when relative permeability is greatest, then attenuation would be expected to decrease in such a natural system. Without a consideration of the poorer sorting, saturation may be overestimated. Whereas sorting in loose sand may not affect velocity variations (Zimmer, Prasad and Mavko 2002), other factors, such as angularity and roughness in natural soils, may promote a decrease in small-strain stiffness, which may follow  $Q$  and even affect the evolution of stress-induced anisotropy (Santamarina and Cho 2004).

## CONCLUSIONS

A publicly available dataset collected from a seismic laboratory experiment shows that *in situ*  $Q$  with depth is sensitive to both stress and water saturation, consistent with  $Q$  trends from core sample resonance studies where  $Q$  increases with stress and reaches a minimum at partial water saturation.

We apply a modified spectral ratio method, which eliminates false  $Q$  values (< 0) and provides well-behaved  $Q$  estimates ( $\pm 0.1$ ). Low  $Q$  values (< 10) may be explained by small matrix elasticities (e.g., < 20 MPa) characteristic of shallow, unconsolidated sediments.

$Q_{int}$  not only shows linear dependence upon stress where dry (e.g., 0.1–0.2 water saturation: 0.0025/Pa,  $r > 0.77$ ) but also at any constant saturation (e.g., 0.6–0.7 water saturation: 0.0013/Pa,  $r > 0.7$ ). Furthermore, minimal  $dQ/dz$  at partial saturation (e.g., dry = 43 m<sup>-1</sup>, partially saturated = 10–13 m<sup>-1</sup>) is interpreted to result from local fluid flow reaching a maximum.  $Q_{int}$  is largest in dry sand and smallest where partially saturated (e.g.,  $Q_{dry} \approx Q_{wet}^{1.4}$ ).  $Q$  deviations outside the range of minimum and maximum  $Q$  values predicted by local fluid flow ( $Q_{dry} \geq Q_{int} \geq Q_{wet}$ ) could be explained by a large change in effective stress, differing attenuation mechanism, or contrasting lithology.

## ACKNOWLEDGEMENT

The authors thank the following for their support with scholarships and a graduate assistantship to the first author: SLFPAAE, API-Delta Chapter—New Orleans, NOGS, SGS, AFMS, SEG, Red River Desk and Derrick Club, Marathon Oil, Chevron Corporation and, especially, to the Louisiana State University Department of Geology & Geophysics for its active support for graduate student research. The authors would also like to thank DOE-LEQSF (2004-7)-L and a Shell E&P Technology Grant for the Sand Tank (2011–2014) that support Lorenzo, White, and Shen. Datasets analysed in this document are downloadable from (<http://github.com/cageo/Lorenzo-2012>). Software (in Perl) used for the analyses is available as an appendix within: [http://etd.lsu.edu/docs/available/etd-08132013-190600/unrestricted/Crane\\_diss.pdf](http://etd.lsu.edu/docs/available/etd-08132013-190600/unrestricted/Crane_diss.pdf) Deep. Considerable time and insight were dedicated during the review process through the efforts of the associate editor and two anonymous reviewers. The authors are very grateful for all their thorough and constructive criticisms.

## REFERENCES

- Aki K. and Richards P.G. 1980. *Quantitative Seismology*. New York, USA: W. H. Freeman and Co.
- Arnold J.G., Srinivasan R., Muttiah R.S. and Williams J.R. 1998. Large area hydrologic modeling and assessment part I: model development. *Journal of the American Water Resources Association* 34(1), 73–89.
- Bachrach R., Dvorkin J. and Nur A. 1998. High-resolution shallow-seismic experiments in sand. Part 2: velocities in shallow unconsolidated sand. *Geophysics* 63(4), 1234–1240.
- Badri M. and Mooney H.M. 1987.  $Q$  measurements from compressional seismic waves in unconsolidated sediments. *Geophysics* 52(6), 772–784.
- Barrière J. Bordes C., Brito D., Sénéchal P. and Perroud H. 2012. Laboratory monitoring of P waves in partially saturated sand. *Geophysical Journal International* 191(3), 1152–1170.
- Båth M. 1974. *Spectral Analysis in Geophysics*. Oxford, UK: Elsevier Science Limited.
- Beard D.C. and Weyl P.K. 1973. Influence of texture on porosity and permeability of unconsolidated sand. *AAPG Bulletin* 57(2), 349–369.
- Binley A., Winship P., Middleton R., Pokar M. and West J. 2001. High-resolution characterization of vadose zone dynamics using cross-borehole radar. *Water Resources Research* 37(11), 2639–2652.
- Biot M.A. 1956. Theory of elastic waves in a fluid-saturated porous solid. 1. Low frequency range. *Journal of the Acoustical Society of America* 28, 168–178.
- Bishop A.W. 1960. *The Principles of Effective Stress*. Norges Geotekniske Institutt.
- Blair D. and Spathis A. 1984. Seismic source influence in pulse attenuation studies. *Journal of Geophysical Research* 89(B11), 9253–9258.
- Brooks R. and Corey A. 1964. *Hydraulic Properties of Porous Media, Hydrology Papers, No. 3*. Ft Collins, Colorado: Colorado State University.
- Cadoret T., Mavko G. and Zinszner B. 1998. Fluid distribution effect on sonic attenuation in partially saturated limestones. *Geophysics* 63(1), 154–160.

- Cerveny V. 2005. *Seismic Ray Theory*. Cambridge, UK: Cambridge University Press.
- Cerveny V., Langer J. and Pšenčík I. 1974. Computation of geometric spreading of seismic body waves in laterally inhomogeneous media with curved interfaces. *Geophysical Journal of the Royal Astronomical Society of London* **38**, 9–19.
- Chilingar G.V. 1964. Relationship between porosity, permeability, and grain-size distribution of sands and sandstones. In: *can Straaten* (ed L.M.J.U.) Deltaic and Shallow Marine Deposits, Developments in Sedimentology 1, 71–74.
- Desbarats A. 1995. Upscaling capillary pressure-saturation curves in heterogeneous porous media. *Water Resource Research* **31**(2), 281–288.
- Dutta N. and Odé H. 1979. Attenuation and dispersion of compressional waves in fluid-filled porous rocks with partial gas saturation (white model)-part I: Biot theory. *Geophysics* **44**(11), 1777–1788.
- Dutta T., Mavko G. and Mukerji T. 2010. Improved granular medium model for unconsolidated sands using coordination number, porosity, and pressure relations. *Geophysics* **75**(2), E91–E99.
- Engel J., Schanz T. and Lauer C. 2005. State parameters for unsaturated soils, basic empirical concepts. In: *Unsaturated Soils: Numerical and Theoretical Approaches* (ed T. Schanz, pp. 125–138. Springer Berlin Heidelberg.
- Engelhard L. 1996. Determination of seismic-wave attenuation by complex trace analysis. *Geophysical Journal International* **125**(2), 608–622.
- Evans B.J. 1997. *A Handbook for Seismic Data Acquisition in Exploration*. Tulsa, OK: Society of Exploration Geophysics.
- Fredlund D.G. and Xing A. 1994. Equations for the soil-water characteristic curve. *Canadian Geotechnical Journal* **31**(4), 521–532.
- Futterman W.I. 1962. Dispersive body waves. *Journal of Geophysical Research* **67**(13), 5279–5291.
- Gassmann F. 1951. Über die Elastizität poroser Medien. *Veierteljahrsschrift der Naturforschenden Gesellschaft in Zurich* **96**, 1–23.
- Van Genuchten, M.T. 1980. A closed-form equation for predicting the hydraulic conductivity of unsaturated soils. *Soil Science Society of America Journal* **44**, 892–898.
- Gillham R.W. 1984. The capillary fringe and its effect on water-table response. *Journal of Hydrology* **67**(1–4), 307–324.
- Haase A.B. and Stewart R.R. 2006. Stratigraphic attenuation of seismic waves. CREWES Research Report, Consortium for Research in Elastic Wave Exploration Seismology, Calgary, Alberta, Canada.
- Haase A.B. and Stewart R. R. 2010. Near-field seismic effects in a homogeneous medium and their removal in vertical seismic profile attenuation estimates. *Geophysical Prospecting* **58**(6), 1023–1032.
- Hamilton E.L. 1976. Sound attenuation as a function of depth in the sea floor. *Journal of the Acoustical Society of America* **59**, 528.
- Jongmans D. 1990. In-situ attenuation measurements in soils. *Engineering Geology* **29**(2), 99–118.
- Knopoff L. 1964. *Q. Reviews of Geophysics* **2**, 625–660.
- Krantz R.W. 1991. Measurements of friction coefficients and cohesion for faulting and fault reactivation in laboratory models using sand and sand mixtures. *Tectonophysics* **188**(1–2), 203–207.
- Lorenzo J.M., Smolkin D.E., White C., Chollett S.R. and Sun T. 2013. Benchmark hydrogeophysical data from a physical seismic model. *Computers and Geosciences* **50**(0), 44–51.
- Mavko G., Mukerji T. and Dvorkin J. 2005. *The Rock Physics Handbook: Tools for Seismic Analysis of Porous Media*. Cambridge, UK: Cambridge University Press.
- Mavko G. and Nur A. 1975 Melt squirt in the asthenosphere. *Journal of Geophysical Research* **80**, 1444–1448.
- Mateeva A. 2003. Quantifying the uncertainties in absorption estimates from VSP spectral ratios. Center for Wave Phenomena—Report 457, 1–14. Colorado School of Mines, Golden, Colorado.
- Mindlin R. 1949. Compliance of elastic bodies in contact. *Journal of Applied Mechanics* **16**.
- Murphy III W.F. 1982. Effects of partial water saturation on attenuation in Massillon sandstone and Vycor porous glass. *Journal of the Acoustical Society of America* **71**, 1458.
- Oelze M.L., O'Brien W.D. and Darmody R.G. 2002. Measurement of attenuation and speed of sound in soils. *Soil Science Society of America Journal* **66**(3), 788–796.
- Petak W.J. and Atkisson A.A. 1982. Natural hazard risk assessment and public policy: anticipating the unexpected. Cambridge, UK: Cambridge University Press.
- Pham N.H., Carcione J.M., Helle H.B. and Ursin B. 2002. Wave velocities and attenuation of shaley sandstones as a function of pore pressure and partial saturation. *Geophysical Prospecting* **50**(6), 615–627.
- Pride S.R. and Berryman J.G. 2003. Linear dynamics of double-porosity dual-permeability materials. I. Governing equations and acoustic attenuation. *Physical Reviews E* **68**(3), 036603.
- Raikes S. and White R. 2006. Measurements of earth attenuation from downhole and surface seismic recordings. *Geophysical Prospecting* **32**(5), 892–919.
- Reine C., van der Baan M. and Clark R. 2009. The robustness of seismic attenuation measurements using fixed-and variable-window time-frequency transforms. *Geophysics* **74**(2), WA123–WA135.
- Santamarina J. and Cho G.C. 2004. Soil behavior: the role of particle shape. *Proceedings of the Skempton Conference*, London, UK, March, pp. 1–14.
- Shen J., Crane J.M., Lorenzo J.M. and White C.D. 2016. Seismic velocity prediction in shallow (<30 m) partially saturated, unconsolidated sediments using effective medium theory. *Journal of Environmental & Engineering Geophysics* **21**(2), 67–78.
- Slotnick M. 1936. On seismic computations, with applications, I. *Geophysics* **1**(1), 9–22.
- Sioseis 2011. A computer system for enhancing and manipulating marine seismic reflection and refraction data. <http://sioseis.ucsd.edu/>, version 2011.3.16 [Accessed 15 Dec. 2011].
- Song Y.-S., Hwang W.-K., Jung S.-J. and Kim T.-H. 2012. A comparative study of suction stress between sand and silt under unsaturated conditions. *Engineering Geology* **124**(0), 90–97.
- Stockwell J.W. 1999. The CWP/SU: Seismic Unix package. *Computers & Geosciences* **25**, 415–419.
- Tarif P. and Bourbie T. 1987. Experimental comparison between spectral ratio and rise time techniques for attenuation measurement. *Geophysical Prospecting* **35**, 668–680.
- Terzaghi K., Peck R.B. and Mesri G. 1996. *Soil Mechanics in Engineering Practice*. Wiley-Interscience.
- Thakur G. 1991. Waterflood surveillance techniques—A reservoir management approach. *Journal of Petroleum Technology* **43**, 1180–1188.
- Toms J., Müller T. and Gurevich B. 2007. Seismic attenuation in porous rocks with random patchy saturation. *Geophysical Prospecting* **55**, 671–678.
- Tonn R. 1991. The determination of the seismic quality factor Q from VSP data: a comparison of different computational methods. *Geophysical Prospecting* **39**, 1–27.
- Turner J.S. 1979. *Buoyancy Effects in Fluids*. Cambridge, UK: Cambridge University Press.

Vincent P.D., Steeples D.W., Tsoflias G.P. and Sloan S.D. 2005. Two approaches to noise tests. SEG technical program, Expanded Abstracts 24, 1180–1183.

Winkler K.W. 1985. Dispersion analysis of velocity and attenuation in Berea sandstone. *Journal of Geophysical Research* **90**(6), 793–796.

Winkler K.W. and Nur A. 1982. Seismic attenuation; effects of pore fluids and frictional sliding. *Geophysics* **47**(1), 2–16.

Wu R.-S. and Aki K. 1988. Introduction: seismic wave scattering in three-dimensionally heterogeneous earth. *Pure and Applied Geophysics* **128**, 1–6.

Wu R.S. 1985. Multiple scattering and energy transfer of seismic waves—separation of scattering effect from intrinsic attenuation—I. Theoretical modelling. *Geophysical Journal of the Royal Astronomical Society of London* **82**, 57–80.

Zimmer M., Prasad M. and Mavko G. 2002. Pressure and porosity influences on VP-VS ratio in unconsolidated sands. *The Leading Edge* **21**, 178–183.